

# Localisation of Gamma Ray Bursts using *AstroSat* Mass Model

Divita Saraogi<sup>1</sup>, <sup>\*</sup> J Venkata Aditya<sup>2</sup>, Varun Bhalerao<sup>1</sup>, <sup>†</sup> Suman Bala<sup>1,3</sup>, Arvind Balasubramanian<sup>4</sup>,  
Sujay Mate<sup>4</sup>, Tanmoy Chattopadhyay<sup>5</sup>, Soumya Gupta<sup>6</sup>, Vipul Prasad<sup>8</sup>, Gaurav Waratkar<sup>1</sup>,  
Navaneeth P K<sup>8</sup>, Rahul Gopalakrishnan<sup>8</sup>, Dipankar Bhattacharya<sup>7</sup>, Gulab Dewangan<sup>8</sup>, Santosh Vadawale<sup>9</sup>

<sup>1</sup>Department of Physics, Indian Institute of Technology Bombay, Powai, Mumbai, Maharashtra 400076, India

<sup>2</sup>Department of Computer Science and Engineering, Indian Institute of Technology Bombay, Powai, Mumbai, Maharashtra 400076, India

<sup>3</sup>Science and Technology Institute, Universities Space Research Association, Huntsville, AL 35805, USA

<sup>4</sup>Department of Astronomy and Astrophysics, Tata Institute of Fundamental Research, Mumbai, Maharashtra 400005, India

<sup>5</sup>Kavli Institute of Astrophysics and Cosmology, Stanford University, 452 Lomita Mall, Stanford, CA 94305, USA

<sup>6</sup>Homi Bhabha National Institute, Anushakti Nagar, Mumbai, Maharashtra 400094, India

<sup>7</sup>Ashoka University, Department of Physics, Sonapat, Haryana 131029, India

<sup>8</sup>Inter University Centre for Astronomy and Astrophysics, Pune, Maharashtra 411007, India

<sup>9</sup>Physical Research Laboratory, Ahmedabad, Gujarat 380009, India

Accepted XXX. Received YYY; in original form ZZZ

## ABSTRACT

The Cadmium Zinc Telluride Imager (CZTI) aboard *AstroSat* has good sensitivity to Gamma Ray Bursts (GRBs), with close to 600 detections including about 50 discoveries undetected by other missions. However, CZTI was not designed to be a GRB monitor and lacks localisation capabilities. We introduce a new method of localising GRBs using ‘shadows’ cast on the CZTI detector plane due to absorption and scattering by satellite components and instruments. Comparing the observed distribution of counts on the detector plane with simulated distributions with the *AstroSat* Mass Model, we can localise GRBs in the sky. Our localisation uncertainty is defined by a two-component model, with a narrow Gaussian component that has close to 50% probability of containing the source, and the remaining spread over a broader Gaussian component with an 11.3 times higher  $\sigma$ . The width ( $\sigma$ ) of the Gaussian components scales inversely with source counts. We test this model by applying the method to GRBs with known positions and find good agreement between the model and observations. This new ability expands the utility of CZTI in the study of GRBs and other rapid high-energy transients.

**Key words:** transients: gamma-ray bursts - software: simulations - software: data analysis - space vehicles: instruments - instrumentation: detectors

## 1 INTRODUCTION

High-energy transients such as Gamma-Ray Bursts (GRBs), soft gamma repeaters (SGRs), X-ray counterparts to fast radio bursts (FRBs), and electromagnetic counterparts to gravitational waves (EMGW) are extraordinary physical phenomena linked to the activities of compact objects like neutron stars and black holes. Recent years have seen increased interest in the search for and study of these high-energy transients due to their association with cosmological sources (Mészáros et al. 2019). Among these phenomena, GRBs stand out as particularly intriguing transient events, releasing an astonishing amount of energy of the order of  $10^{51}$  to  $10^{54}$  erg (Piron 2016). The initial prompt emission during a GRB occurs within a brief duration, typically ranging from a fraction of a second to a few minutes — or even thousands of seconds in the longest cases (Zhang 2014; von Kienlin et al. 2020a; Lien et al. 2016). However,

the brevity and uncertain positional information of these events make their study challenging.

GRBs have been a subject of study for several decades. To track the afterglow of GRBs, numerous ground-based telescope networks have been established, complementing space-based instruments that initially detect the prompt emission for initial localisation. Survey telescopes like Panoramic Survey Telescope and Rapid Response System (PAN-STARRS; Chambers et al. 2016) and the Zwicky Transient Facility (Bellm 2014) diligently follow up on transients and relay transient alerts through Astronomers Telegram (Hložek 2019). Additionally, global radio telescopes, including Very Long Baseline Interferometry (VLBI; Chandra 2016; Mundell et al. 2010), conduct follow-up studies of these transients. By studying transients across different wavelength bands, a comprehensive understanding of the GRB emission mechanism can be achieved, aiding the development and refinement of theoretical models.

The detection of GRB 170817A — the gamma ray burst associated with the gravitational wave event GW170817 along with the gravitational wave detection by Laser Interferometer Gravitational-wave Observatory (LIGO) has given birth to multi-messenger astronomy

<sup>\*</sup> E-mail: divitadsaraogi@gmail.com

<sup>†</sup> E-mail: varunb@iitb.ac.in

(Abbott et al. 2017). The detection of this GRB by *Fermi* (Goldstein et al. 2017) coincident with the gravitational wave signal spurred a flurry of multi-wavelength observations that led to detailed characterisation of this event. While *Fermi* (Goldstein et al. 2017) and *Integral* (Savchenko et al. 2017) detected this burst, it was missed by *Swift* and *AstroSat* which were sensitive enough to detect it as it was occulted by the Earth (Evans et al. 2017; Kasliwal et al. 2017). The non-detection by CZTI despite the flux being above the detection threshold proved the Earth-occulted scenario and aided in narrowing down the source localisation by a factor of two (Kasliwal et al. 2017). Detection and localisation of high-energy bursts has at times changed the complete interpretation of an event. The discovery of GRB 170105A and its localisation were key in proving that the orphan afterglow ATLAS17aeu was associated with this GRB and not the binary black hole merger GW170104 (Bhalerao et al. 2017b). *AstroSat*-CZTI has been detecting a large number of bursts and can be used to measure the polarisation of bright bursts (Chattopadhyay et al. 2019; Chattopadhyay et al. 2022). However, polarisation analysis requires the knowledge of the source position in the sky, failing which the analysis cannot be completed. Two examples of such bursts are GRB 200503A (Gupta et al. 2020a) and GRB 201009A (Gupta et al. 2020b). While they were also detected by other spacecraft like *AGILE* (Ursi et al. 2020a,b), *Konus-Wind* (Hurley, private communication), the sources were not well-localised by any of them. This has prevented us thus far from making two valuable additions to the rather small number of GRBs with measured polarisation.

Astronomical X-ray instruments employ various methods for source localisation. One approach involves projection-based localisation, where the number of counts observed by different detectors of the same instrument facing different directions is compared. This technique is used by missions such as *Fermi*-GBM (Connaughton et al. 2015), *CGRO*-BATSE (Meegan et al. 1992), *GECAM* (Xin-Ying et al. 2020), and the upcoming *Daksha* mission (Bhalerao et al. 2022a), providing localisations within a few degrees. Another method utilizes a coded aperture mask (CAM) to achieve enhanced localisation accuracy of the order of a few arc minutes. Instruments like *Swift*-BAT (Barthelmy et al. 2005), *INTEGRAL* (Mereghetti et al. 2004), and *ECLAIRS* onboard the *SVOM* mission (Triou et al. 2009) utilize CAM for GRB localisation, but this improved localisation typically comes at the cost of a limited field of view. Additionally, the interplanetary network (IPN) technique, involving data from different satellites (Hurley et al. 2013; Hurley 2020), enables GRB localisation by leveraging the separation and arrival time of bursts on multiple satellites.

To localise GRBs with *AstroSat*-CZTI, earlier attempts have been made by using ray-trace simulations which is an analytical method calculating the shadow (i.e. the degree of absorption and transmission) cast by different components of CZTI on the detector, for photons of given energy and direction of incidence and predict the effective area of the same (Bhalerao et al. 2017b). However, this method ignores the absorption or scattering contributions of the rest of the satellite, and hence is rather limited in its accuracy and the fraction of the sky where it is applicable. Hence, to localise the GRBs we present a method that uses the shadow cast by other instruments, allowing us to determine the GRB location by comparing the observations with simulations obtained using the *AstroSat* Mass Model (Mate et al. 2021). In this paper, we present the localisation results obtained by analyzing a sample of GRBs detected by *AstroSat*-CZTI, using the *AstroSat* Mass Model to localise these GRBs and validate our results using localisation information from other instruments like *Fermi*, *Swift* or Interplanetary network (IPN).

This paper is structured in the following fashion: We briefly de-

scribe the *AstroSat*-CZTI instrument and the Mass Model in section §2. The framework for localising GRBs using the *AstroSat* Mass Model is discussed in section §3. The localisation results for our GRB sample and the calculation of uncertainty on the result are discussed in section §4. In section §5, we summarize our results and describe the impact of our results on future work.

## 2 TRANSIENTS WITH *AstroSat*-CZTI

*AstroSat* is India's first multi-wavelength mission that carries instruments covering the energy range from ultraviolet to high-energy X-rays (Singh et al. 2014). The five principal scientific payloads onboard *AstroSat* are: (i) a Soft X-ray Telescope (SXT), (ii) three Large Area Xenon Proportional Counters (LAXPCs), (iii) a Cadmium-Zinc-Telluride Imager (CZTI), (iv) an Ultra-Violet Imaging Telescope (UVIT) configured as two independent telescopes, and (v) a Scanning Sky Monitor (SSM). The CZTI instrument onboard *AstroSat* is a high-energy X-ray instrument providing wide-field coverage. CZTI contains 64 detectors with 256 pixels each, arranged in a square pattern to obtain nearly 1000 cm<sup>2</sup> geometric area (Bhalerao et al. 2017a). Collimators limit the primary field of view to approximately 4.6°, but these become increasingly transparent to radiation above 100 keV. This, combined with the 20–200 keV sensitive energy range makes CZTI an excellent all-sky detector for high-energy transients. CZTI was not designed as a GRB detection instrument, but over the years of its operation, it has proven very successful in detecting a large number of GRBs (Sharma et al. 2021). In the 7 years of its operation *AstroSat* has detected close to 600 GRBs<sup>1</sup>. *AstroSat* has also proven very successful in measuring the polarisation of GRBs, having studied 20 GRBs so far (Chattopadhyay et al. 2022).

As *AstroSat* can detect off-axis GRBs but does not have localisation capability, it has thus far relied on other GRB detection instruments for localisation information. The localisation method presented here can overcome this hurdle.

The *AstroSat* Mass Model is a numerical model of the satellite body, created using GEANT4<sup>2</sup> (Agostinelli et al. 2003), a tool for simulating interactions of photons and particles with matter. The details of *AstroSat* Mass Model can be found in Mate et al. (2021), hereafter referred to as MM21. We use the Mass Model to simulate the interaction of the incoming GRB photons with the satellite elements. Photons from a source incident on the satellite body may get transmitted, scattered, or absorbed and re-emitted with new energies and directions. All these effects lead to a direction-dependent ‘image’ on the detectors, which we term a ‘Detector Plane Histogram’ (DPH). Numerical calculations with the mass model can be used to simulate this DPH as a function of source direction. Thanks to the inhomogeneous distribution of satellite elements around the CZTI detectors, the DPH is different for each source direction. Thus, we can use the observed DPH for any GRB and compare it with a library of simulated DPHs to infer the location of the source in the sky. This principle is used to localise GRBs.

## 3 LOCALISATION USING MASS MODEL

In our localisation approach, we employ simulations generated by the *AstroSat* Mass Model at various positions in the sky. These sim-

<sup>1</sup> <http://astrosat.iucaa.in/czti>

<sup>2</sup> <http://geant4.web.cern.ch/geant4/>

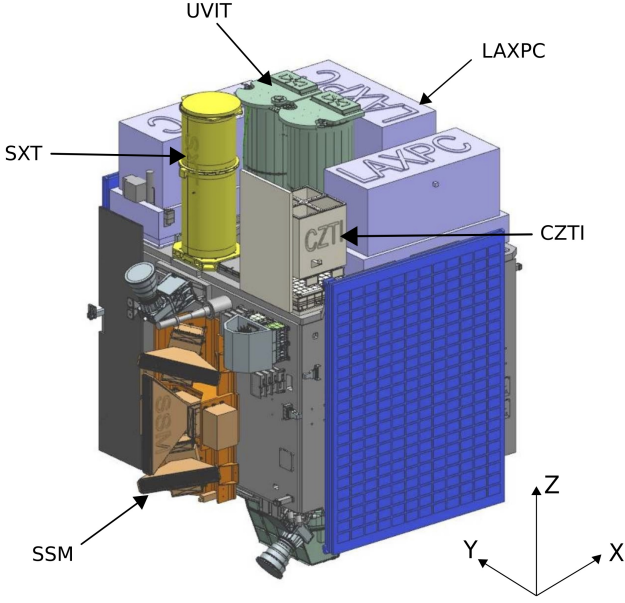


**Figure 1.** Representative CAD model of *AstroSat* with folded solar panels, featuring the five payloads of *AstroSat*, and displaying the coordinate axes for CZTI.

ulations yield a DPH giving the expected number of photons in each of the 16,384 pixels of CZTI. This simulated DPH can then be compared with the observed background-subtracted DPH of a GRB. We bin the pixel data to perform a module-wise comparison between the observed data to the simulated DPH, as given by Equation 1:

$$\chi^2 = \sum_{m=1}^{64} \frac{(N_{\text{sim},m} - N_{\text{src},m})^2}{\sigma_{\text{sim},m}^2 + \sigma_{\text{src},m}^2} \quad (1)$$

where the summation is carried out over all 64 modules and on an average each module has more than 60 counts. The uncertainties in the simulated DPH are calculated as described in MM21. The GRB window  $t_{\text{src}}$  contains  $N_{\text{obs},m}$  counts from the GRB as well as background. We calculate the source counts and uncertainty as follows:

$$N_{\text{src},m} = N_{\text{obs},m} - N_{\text{bkg},m} \times \frac{t_{\text{src}}}{t_{\text{bkg}}} \quad (2)$$

$$\sigma_{\text{src},m}^2 = N_{\text{obs},m} + N_{\text{bkg},m} \times \left( \frac{t_{\text{src}}}{t_{\text{bkg}}} \right)^2 \quad (3)$$

The background  $N_{\text{bkg},m}$  is measured using a longer window  $t_{\text{bkg}}$  and scaled before subtracting, in order to reduce the uncertainty contribution. The uncertainties in source and background are calculated assuming Poisson statistics. Repeating this procedure over the entire sky, the global minimum of  $\chi^2$  gives the best-fit position of the source. As discussed in MM21, in practice it has been seen that there can be an overall scaling factor needed to make the GRB fluence match with the observed counts, and an offset factor to correct for any background subtraction residuals. Following MM21, we allow for additive and multiplicative scaling factors while calculating the  $\chi^2$  values for each direction in our grid. As an example, Figure 2 shows the source DPH for GRB 190117A, compared with our simu-

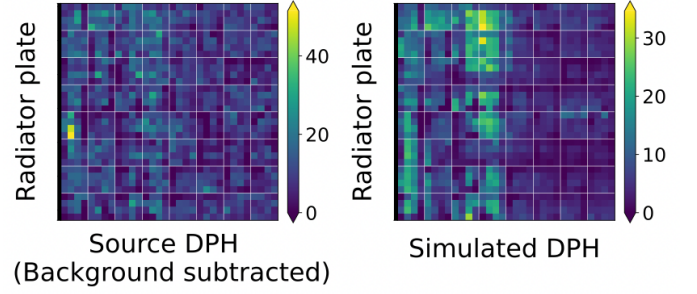


**Figure 2.** Comparing detector plane histograms (DPHs) for GRB 190117A. The left figure shows the observed background-subtracted DPH. The right side shows the scaled simulated DPH for a source located at the closest HTM grid point to the actual GRB position. The left image is more “grainy” due to the small number of statistics in observed data.

lated DPH for the closest grid point to the true GRB location on the sky.

For localisation, we need simulations uniformly distributed over the entire sky. The selection of such points can be conveniently done using grids like the Hierarchical Triangular Mesh (HTM) (Kunszt et al. 2001) or Healpix (Gorski et al. 2005). For this work, HTM offers a distinct advantage: as we refine the resolution of HTM pixels, the centres of pixels from a coarse grid also become points on a finer grid. This allows us to refine our grid in selected parts of the sky without disrupting the grid pattern. Healpix, on the other hand, does not share this property. Hence, we opt to forgo the Healpix grid and instead pick an HTM grid of an appropriate resolution.

Based on simulations, we concluded that we need a grid resolution of  $\sim 5^\circ$ . This corresponds to a ‘Level 4’ HTM grid with pixel centres separated by  $5.62^\circ$ , having a total of 2048 pixels in the sky. We generated the Level 4 HTM grid in satellite  $\theta$ - $\phi$  coordinates, where  $\theta$  is measured from the Z-axis and  $\phi$  is measured from the X-axis along the XY plane (Figure 1). We then undertook GEANT4 Mass Model simulations at each of those points. Since each GRB can have a different spectrum, we opted to simulate DPHs for monochromatic incident photons at 197 energies ranging from 20 keV – 2 MeV, with an adaptive step size based on energy resolution. The simulations commence at 20 keV, with increments of 5 keV up to 500 keV. In the range of 500 keV to 1 MeV, the step size is increased to 10 keV, followed by 20 keV steps in the 1 MeV to 2 MeV range. As discussed in MM21, photons up to about 2 MeV can make significant contributions in the 20–200 keV range. At each energy level, we simulate the interaction of 6.97 million incident photons with the entire satellite. This simulation is carried out by employing a circular source plane with a radius of 200 cm, resulting in a photon flux of  $55.46 \text{ photons cm}^{-2}$  as outlined in MM21. To carry out these simulations, we harnessed the high-performance computing cluster at IUCAA, Pune<sup>3</sup>, leveraging 16 nodes, each equipped with 512 cores, which collectively accumulated to approximately  $10^5$  CPU-hours.

The DPHs are then weighted by the spectrum of the incident GRB and summed to create the final simulated DPH for that direction. In cases where the GRB spectrum is unknown, we proceed with standard *Fermi* spectral parameters from Nava et al. (2011). Once the location is known, in principle, the mass model can be used to fit the GRB spectrum, which can be used iteratively to improve the

<sup>3</sup> <http://hpc.iucaa.in/>



location. Such iterative or joint fitting is beyond the scope of this work and will be addressed in a separate future work.

As an example, we show the  $\chi^2$  contours for GRB 190117A in Figure 3. The best-fit position is then simply taken as the grid point having the lowest  $\chi^2$  value. We note that the finite grid size means that even for the brightest GRB our  $\theta$  offset will be as large as half of the grid size i.e. about  $2.81^\circ$  or about the area of a pixel which is  $20.14 \text{ deg}^2$ .

## 4 METHOD

### 4.1 GRB sample

To validate our localisation results we select a sample of 29 bright GRBs detected by *AstroSat* before May 2023 and compare the results with the Mass Model simulations. The selection criterion for this sample is that the total GRB counts in the data should be  $\geq 4000$  and the localisation information should be available from other missions like *Fermi*, *Swift*, *Maxi*, and IPN so that we can validate our localisation results. We converted the RA, and Dec obtained from these instruments to the  $\theta - \phi$  coordinates in the CZTI frame. For these GRBs, the spectral parameters are obtained from either *Fermi* or *Konus-Wind*, and we scale the normalization values in the energy range from 70 – 200 keV, which is the energy range in which we perform all our analyses for *AstroSat*-CZTI. One source we do not consider in our sample is GRB 160325A which was detected with 19229 counts. It was incident nearly on-axis for CZTI, where accurate localisation is done using the coded aperture mask (Vibhute et al. 2021). On the other hand, the Mass Model makes certain approximations which make it relatively less accurate for on-axis sources. Hence, we exclude this GRB from our sample.

### 4.2 Localisation contours

As discussed in §3, we calculate the  $\chi^2$  for all directions for our GRB sample. We exclude the part of the sky that was occulted by the earth as seen from the satellite at the instant of the burst. Sample localisation contours are shown in Figure 3. The left column shows the contours plotted in RA-Dec coordinates, viewed from three different directions in the sky. The right column shows three views of contours plotted in  $\theta - \phi$  coordinates. Where visible, the location of the GRB is marked with a cross.

Inspecting the contours created for our entire sample, we observe that in most of the cases, the source is well localised with contours showing a single global minimum, while in other cases there are multiple local minima with comparably low  $\chi^2$  values. In some of these cases, the actual GRB location is closer to a secondary minimum rather than the global minimum. This suggests that we should select a “contour filling” method for describing the GRB location, rather than simply giving an angular offset.

For our 29-GRB sample, we have prior knowledge of the actual source location from other observational instruments. We approximate the GRB position with the HTM grid point closest to it. We denote the  $\chi^2$  value at this grid position (cgp) by  $\chi_{\text{cgp}}^2$ . Subsequently, we determine the number of grid points in our analysis that possess  $\chi^2$  values less than  $\chi_{\text{cgp}}^2$ . The total area with  $\chi^2 < \chi_{\text{cgp}}^2$  is designated as the “enclosed area”  $A_e$ . In Table 2, we provide the obtained values of  $A_e$  for each GRB in our dataset. Thus, the enclosed area  $A_e$  is the smallest two-dimensional region, originating from regions with the highest likelihood, that encompasses the true source location.

### 4.3 Uncertainties in Localisation

Our localisation method is broadly similar to the source localisation by *Fermi*-GBM or by the proposed *Daksha* mission. In these cases, it is seen that the uncertainty in the localisation area scales inversely as the detected counts in GRBs detected by GBM (von Kienlin et al. 2020a) and simulations for *Daksha* (Bhalerao et al. 2022b). On the other hand, we can also treat the spacecraft elements as a coded aperture mask being used to obtain source positions. For coded aperture instruments, the localisation position uncertainty scales inversely as SNR (Baumgartner et al. 2013). For bright bursts that we discuss, SNR scales as  $\sqrt{\text{counts}}$ , and again area uncertainty would scale inversely to the observed counts. Thus, we postulate that the localisation area will scale inversely with the observed counts as,

$$A_{50} = \frac{K_a}{\text{counts}} \quad (4)$$

Where  $K_a$  is a constant, and  $A_{50}$  is defined as the area on the sky that has a 50% probability of enclosing the true location of the source.

If we had a large number of GRBs with the same counts then we could have created a distribution of the offsets and calculated  $A_{50}$  as the median, thus giving us a value of  $K_a$  from Equation 4. However, in practice our GRB sample has different counts for each source, and hence different values for  $A_{50}$ . To overcome this limitation, we measure the enclosed area  $A_e$  for each GRB and normalise it by the expected  $A_{50}$  for that source getting a new variable, the “normalised area” defined as  $a = A_e/A_{50}$ . The distribution of ‘ $a$ ’ gives the probability distribution function of our uncertainties.

To evaluate this underlying probability distribution, we create a cumulative plot of the normalised area (Figure 4). For normally distributed uncertainties, this should yield an error function (erf). We can see that there is a sharply concentrated core of well-localised GRBs, but we also have a large number of outliers. We find that this is well modelled as a sum of two Gaussians: a narrow component and a broad component with standard deviations  $\sigma_1$  and  $\sigma_2$  respectively. The corresponding cumulative distribution function is given by Equation 5, where  $f$  is the fractional contribution of the broad component.

$$cdf(a) = \int_0^a f \frac{1}{\sigma_1 \sqrt{2\pi}} e^{-x^2/2\sigma_1^2} + (1-f) \frac{1}{\sigma_2 \sqrt{2\pi}} e^{-x^2/2\sigma_2^2} dx \quad (5)$$

This distribution gives a good fit to observed data, with  $\sigma_1 = 0.42$ ,  $\sigma_2 = 4.76$  and  $f = 0.59$ . We require that the median of this distribution occurs at  $a = 1$ , yielding  $K_a = 6.87 \times 10^6$ . For these distributions, the enclosed probability for various values of  $a$  is given in Table 1.

We investigated the GRBs to look for any patterns among GRBs that better line up with the narrow versus broad components of the distribution. We find that for GRBs above/below the detector plane ( $\theta < 60^\circ$  or  $\theta > 90^\circ$ ), the  $\phi$  values are often correctly measured, and the discrepancy in  $\theta$  can be large, even upto  $60^\circ$ . Additional minima are usually seen close to the detector plane ( $60^\circ < \theta < 120^\circ$ ), where the DPHs become relatively featureless. An illustration can be seen in Figure 3, where the lower right panel shows two broad local minima above and below the  $\theta = 90^\circ$  detector plane. However, for this GRB the global minimum happens to be deeper than these spurious local minima, thus giving good localisation. On the other hand, for GRBs close to the detector plane ( $60^\circ < \theta < 120^\circ$ ), we find that the algorithm correctly places the GRBs within this  $\theta$  range, but can have larger errors in both  $\theta$  and  $\phi$ . This effect was also seen in MM21, the relatively featureless nature of the DPH resulted in poorer fits between simulations and observations. The effect can be

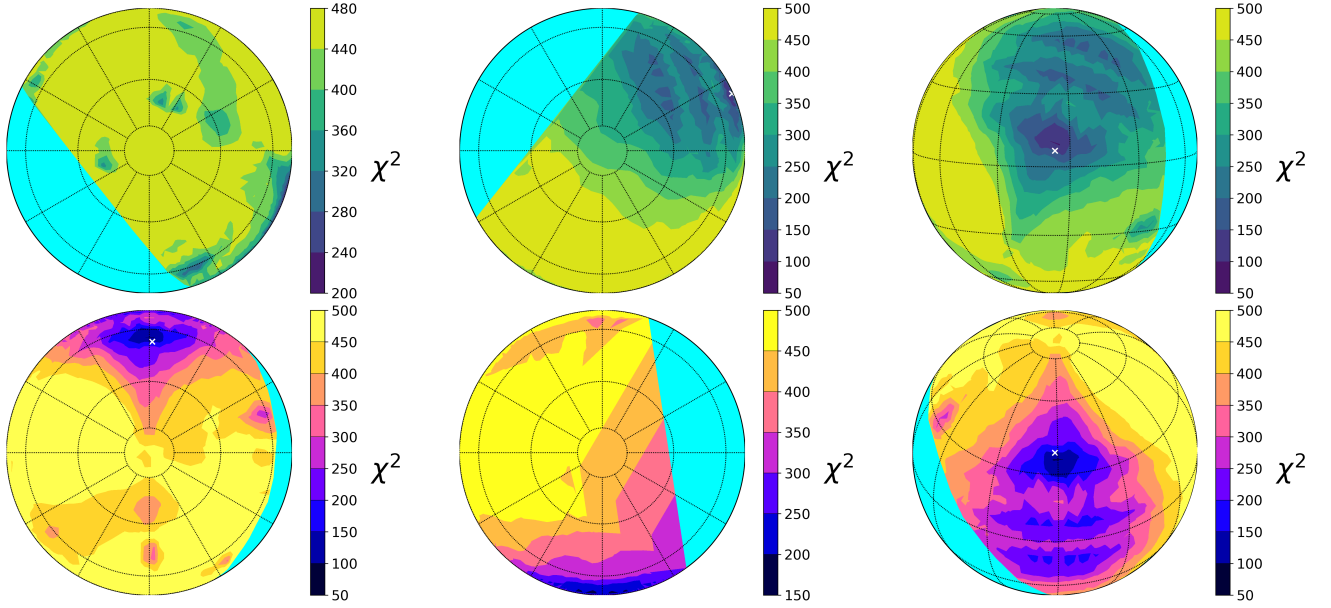


**Figure 3.** All-sky  $\chi^2$  contour plots for GRB 190117A, as viewed from various directions in different coordinate systems. The top panel shows contour plots in the RA—Dec coordinate system, with the three figures showing views from RA, Dec = (0, −90), (0, 90), and (113.86, 6.51) from left to right. The three figures in the bottom panel show contours in the satellite  $\theta$ — $\phi$  coordinates, as viewed from  $\theta$ ,  $\phi$  = (0, 0), (180, 0), and (51.26, 178.51) from left to right. The rightmost figure in each row is a view from the direction of the transient. The darkest region in the contour plot is the most likely location of the GRB from our fits. Where visible, the true location of the GRB is marked with a white cross.

**Table 1.** Probability of contained area and corresponding normalised area.

Contained probability	Normalised area
0.10	0.12
0.20	0.24
0.30	0.39
0.40	0.59
0.50	1.00
0.60	1.98
0.70	3.16
0.80	4.56
0.90	6.55

mitigated to some extent if we know the coarse localisation of the GRBs from other sources — in which case we can focus only on the relevant local minimum, yielding better localisation. The details of this are not explored further in this work.

## 5 RESULTS AND DISCUSSIONS

Under the current counts cutoff criterion of 4000 counts, we successfully localized 29 GRBs within the dataset spanning a period of 7 years. The GRBs in our sample have minimum fluence  $5.76 \times 10^{-6} \text{ erg cm}^{-2} \text{ s}^{-1}$  and maximum fluence  $6.60 \times 10^{-4} \text{ erg cm}^{-2} \text{ s}^{-1}$ . Hence, we can localise GRBs with a minimum fluence of  $\sim 6 \times 10^{-6} \text{ erg cm}^{-2} \text{ s}^{-1}$  to an approximate area  $A_{50} \approx 1700 \text{ sq. degree}$ .

This method is now being used to localize bright GRBs detected by *AstroSat*-CZTI. As an illustrative case, consider the recent

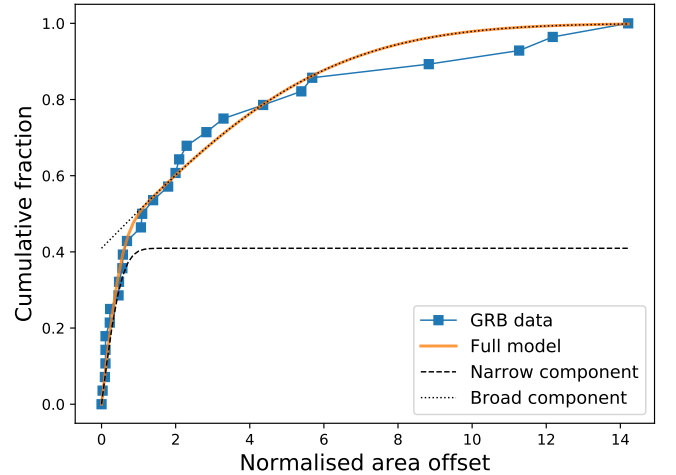


**Figure 4.** This figure presents the cumulative distribution of normalized area offsets for both GRB data and simulations. The data is modelled using a two-component model comprising a narrow and a broad component, with fitted values of  $\sigma_1 = 0.42$ ,  $\sigma_2 = 4.76$ , and  $f = 0.59$ , where  $f$  represents the fractional contribution of the broad component.

GRB 230817A detected by CZTI with 3083 counts, which we localized using our current method. The localisation obtained by *Fermi* for this GRB provided RA = 325.9, Dec = 14.2, and an uncertainty radius of  $3.3^\circ$  (Fermi GBM Team 2023). Our own localisation placed it at RA = 320.35, Dec = 17.53, with a corresponding enclosed area  $A_e = 201.43 \text{ square degree}$ . This is well within the expected uncertainty given by Equation 4,  $A_{50} = 2229.7 \text{ square degree}$ . The

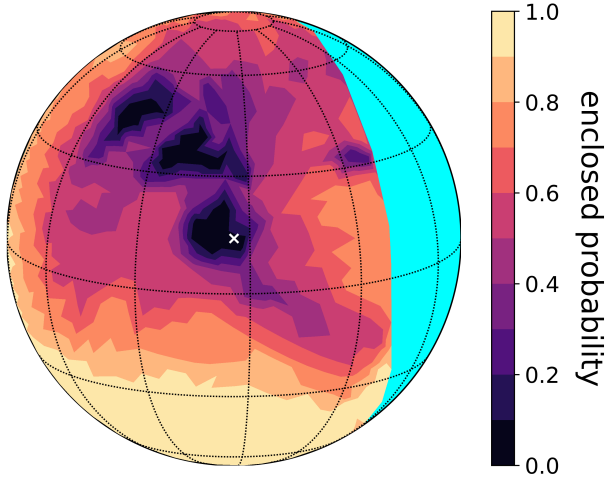


**Figure 5.** All-sky enclosed probability contour plot for GRB 230817A in RA, Dec; the white cross shows the actual position of the GRB. The cyan-coloured region is the region occulted by the earth.

RA-Dec all-sky probability contour plot for this GRB is depicted in Figure 5.

Our preliminary tests have shown that this method extends well to the localisation of GRBs with fewer counts. This highlights the versatility of our approach, rendering it suitable for localizing GRBs detected by other instruments, particularly in situations where the satellite’s structural complexity presents challenges. Currently, this method is being employed to localize two specific GRBs, namely GRB 200503A and GRB 201009A, which will facilitate subsequent polarisation analysis of these events.

The integration of GRB localisation into the *AstroSat*-CZTI GRB pipelines is currently underway, and localisation for bright GRBs will be communicated through future announcements.

## ACKNOWLEDGEMENTS

We thank Prof. A R Rao for useful discussions and guidance. We thank the *AstroSat* CZTI team for the help, support and resources.

CZTI–Imager is the result of a collaborative effort involving multiple institutes across India. The Tata Institute of Fundamental Research in Mumbai played a central role in spearheading the instrument’s design and development. The Vikram Sarabhai Space Centre in Thiruvananthapuram contributed to electronic design, assembly, and testing, while the ISRO Satellite Centre (ISAC) in Bengaluru provided expertise in mechanical design, quality consultation, and project management. The Inter University Centre for Astronomy and Astrophysics (IUCAA) in Pune was responsible for the Coded Mask design, instrument calibration, and the operation of the Payload Operation Centre. The Space Application Centre (SAC) in Ahmedabad supplied the essential analysis software, and the Physical Research Laboratory (PRL) in Ahmedabad contributed the polarization detection algorithm and conducted ground calibration. Several industries were actively involved in the fabrication process, and the university sector played a crucial role in testing and evaluating the payload. The Indian Space Research Organisation (ISRO) not only funded the project but also provided essential management and facilitation throughout its development. We also extend our appreciation for the use of the Pegasus High-Performance Computing (HPC) resources

at the Inter University Centre for Astronomy and Astrophysics (IUCAA) in Pune. This work utilised various software including Python, AstroPy (Robitaille et al. 2013), NumPy (Harris et al. 2020), Matplotlib (Hunter 2007), IDL Astrolib (Landsman 1993), FTOOLS (Blackburn 1995), C, and C++.

**Table 2.** GRB parameters and computed offsets for the GRBs utilized in Localisation Analysis. Abbreviations: SX - *Swift*-XRT, SB - *Swift*-BAT, F - *Fermi*-GBM, I - IPN, M - *Maxi*, C - *Fermi* Catalogue, K - *Konus-Wind*. Spectral parameters are sourced from either *Fermi* GBM or *Konus-Wind*.

GRB name	Actual				Best fit				Instrument		GRB counts	CZTI localisation			References
	RA	Dec	$\theta$	$\phi$	RA	Dec	$\theta$	$\phi$	localisation	spectra		$A_e$	$A_{50}$	a	(localisation,spectrum)
GRB 180809B	299.69	-15.29	26.45	198.88	3.92	36.66	106.08	202.99	SX	K	19662	201.43	349.61	0.57	Liu et al. (2018),Svinkin et al. (2018)
GRB 170527A	195.19	0.94	26.53	101.54	204.91	-4.94	27.8	126.43	F	K	13290	1188.43	517.22	2.29	Stanbro et al. (2017), Frederiks et al. (2017)
GRB 200311A	204	-49.7	30.91	157.64	204.87	-45.06	35.34	154.89	F	K	6102	120.85	1126.40	0.10	Fermi GBM Team (2020), Ridnaia et al. (2020)
GRB 200412A	140.01	-41.67	36.15	270.08	107.91	20.68	105.14	266.03	F	F	6176	100.71	1113.05	0.09	Kunzweiler et al. (2020), Mailyan et al. (2020)
GRB 180914A	53.08	-5.62	40.67	216.51	353.55	-49.83	106.66	225	SX	K	13567	705	506.67	1.39	D'Elia et al. (2018), Tsvetkova et al. (2018)
GRB 180427A	283.33	70.3	40.81	257.79	294.05	5.93	105.14	266.03	F	F	8366	564	303.12	1.86	Bissaldi (2018a),Bissaldi (2018b)
GRB 190117A	113.86	6.51	51.26	178.51	115.73	8.69	54	177.48	F	K	6038	0	1138.44	0	Hurley et al. (2019a), Frederiks et al. (2019a)
GRB 160802A	35.29	72.69	52.95	273.11	20.67	71.47	54	267.48	F	F	12255	60.42	560.89	0.10	Bissaldi (2016a), Bissaldi (2016b)
GRB 180806A	11.55	24.33	54.69	264.49	12.39	26.73	54	267.48	SX	F	4191	100.71	1639.94	0.06	Gibson et al. (2018), Malacaria et al. (2018)
GRB 190731A	339.72	-76.57	57.44	126.29	113.1	-53.72	55.62	69.97	SX	F	9187	3263.17	748.21	4.36	Fermi GBM Team (2019), Roberts et al. (2019)
GRB 190928A	36.57	29.46	57.68	231.25	30.79	26.37	54.74	225	I	K	24175	302.14	284.34	1.06	Hurley et al. (2019b), Frederiks et al. (2019b)
GRB 221209A	241.7	48.1	58.4	310.81	216.85	7.15	104.46	310.55	F	F	4598	705	1494.97	0.47	Fermi GBM Team (2022c), Bissaldi & Fermi GBM Team (2022)
GRB 160910A	221.44	39.06	65.53	333.46	105.72	63.45	105.42	280.06	SX	F	5315	7352.21	1293.16	5.68	Veres & Meegan (2016a), Veres & Meegan (2016b)
GRB 220408B	94.8	-50.9	73.03	275.64	88.26	-49.23	74.58	280.06	F	F	4838	40.28	1420.83	0.03	Fermi GBM Team (2022a), Bissaldi et al. (2022)
GRB 210204A	117.08	11.4	75.28	166.59	145.81	3.88	64.12	195.73	SX	F	7859	201.43	874.69	0.23	Fermi GBM Team (2021), Bissaldi & Fermi GBM Team (2021)
GRB 230204B	197.64	-21.71	76.01	253.9	245.03	-43.73	99.98	292	SX	F	15725	2356.73	437.15	5.39	D'Elia et al. (2023), Poolakkil et al. (2023)
GRB 221022B	167.4	15.4	77.19	312.96	104.01	41.8	93.83	254.83	F	F	6755	12387.97	1017.54	12.17	Fermi GBM Team (2022b), Poolakkil et al. (2022)
GRB 181222A	270.73	-38.84	79.78	346.37	274.59	-31.9	86.2	350.53	M	F	6205	3645.89	1107.84	3.29	Sakamaki et al. (2018), Veres & Bissaldi (2018)
GRB 210822A	304.43	5.27	84.75	168.11	206.6	-1.9	56.73	65.01	SX	K	5504	1369.72	1248.89	1.09	Page et al. (2021), Frederiks et al. (2021)
GRB 201216C	16.37	16.51	88.6	116.81	19.83	17.87	87.98	120.34	SX	F	7212	100.71	953.16	0.10	Beardmore et al. (2020), Malacaria et al. (2020)
GRB 170607B	257.1	-35.7	96.33	178.63	257.48	-8.27	70.63	188.36	F	F	4703	3061.74	1461.37	2.09	Hamburg et al. (2017a), Hamburg et al. (2017b)
GRB 160106A	181.6	17.5	106.09	255.65	165.47	-0.19	129.84	256.61	C	F	4229	2920.74	1625.21	1.79	von Kienlin et al. (2020b), von Kienlin et al. (2020b)
GRB 160607A	13.66	-4.94	138.84	315.76	343.28	42.15	91.91	283.2	SX	F	4867	2820.02	1412.24	1.99	Ukwatta et al. (2016), Tsvetkova et al. (2016)
GRB 160623A	315.29	42.22	140.46	118.06	20.18	-7.38	74.13	73.49	SX	K	11414	5317.76	602.23	8.83	Mingo et al. (2016), Frederiks et al. (2016)
GRB 171010A	66.58	-10.46	142.51	242.01	71.72	-6.31	137.37	248.36	SX	F	39144	80.57	175.61	0.45	D'Ai et al. (2017), Poolakkil & Meegan (2017)
GRB 170906A	203.99	-47.12	146.24	263.16	219.49	-61.73	132.64	247.06	SX	F	5812	664.72	1182.71	0.56	Siegel et al. (2017), Hamburg & Meegan (2017)
GRB 171227A	280.7	-35	146.48	353.57	228.7	37.56	59.68	2.34	F	F	7367	10514.67	933.03	11.26	Hui (2017a), Hui (2017b)
GRB 190530A	120.53	35.47	154.5	79.86	259.8	79.62	91.91	76.8	SX	F	11630	8399.65	591.053	14.21	Biltzinger et al. (2019), Bissaldi & Meegan (2019)
GRB 160821A	171.24	42.34	156.17	59.26	23.07	61.15	88.11	97.52	SB	F	21459	906.43	320.34	2.82	Siegel et al. (2016), Stanbro & Meegan (2016)

**DATA AVAILABILITY**

The data underlying this article will be shared on reasonable request to the corresponding author.

**REFERENCES**

- Abbott B. P., et al., 2017, *The Astrophysical Journal Letters*, 848, L13
- Agostinelli S., et al., 2003, Nuclear instruments and methods in physics research section A: Accelerators, Spectrometers, Detectors and Associated Equipment, 506, 250
- Barthelmy S. D., et al., 2005, *Space Science Reviews*, 120, 143
- Baumgartner W. H., Tueller J., Markwardt C. B., Skinner G. K., Barthelmy S., Mushotzky R. F., Evans P. A., Gehrels N., 2013, *ApJS*, 207, 19
- Beardmore A., et al., 2020, GRB Coordinates Network, 29061, 1
- Bellm E., 2014, in *The Third Hot-wiring the Transient Universe Workshop*.
- Bhalerao V., et al., 2017a, *Journal of Astrophysics and Astronomy*, 38, 1
- Bhalerao V., et al., 2017b, *The Astrophysical Journal*, 845, 152
- Bhalerao V., et al., 2022a, arXiv preprint arXiv:2211.12055
- Bhalerao V., et al., 2022b, *arXiv e-prints*, p. arXiv:2211.12055
- Biltzinger B., Kunzweiler F., Berlato F., Burgess J., Greiner J., 2019, GRB Coordinates Network, 24677, 1
- Bissaldi E., 2016a, GRB Coordinates Network, 19754, 1
- Bissaldi E., 2016b, GRB Coordinates Network, 19754, 1
- Bissaldi E., 2018a, GRB Coordinates Network, 22678, 1
- Bissaldi E., 2018b, GRB Coordinates Network, 22678, 1
- Bissaldi E., Fermi GBM Team 2021, GRB Coordinates Network, 29393, 1
- Bissaldi E., Fermi GBM Team 2022, GRB Coordinates Network, 33034, 1
- Bissaldi E., Meegan C., 2019, GRB Coordinates Network, 24692, 1
- Bissaldi E., Meegan C., Fermi GBM Team 2022, GRB Coordinates Network, 31906, 1
- Blackburn J. K., 1995, *Astronomical Data Analysis Software and Systems IV*, 77
- Chambers K. C., et al., 2016, arXiv preprint arXiv:1612.05560
- Chandra P., 2016, *Advances in Astronomy*, 2016
- Chattopadhyay T., et al., 2019, *ApJ*, 884, 123
- Chattopadhyay T., et al., 2022, *The Astrophysical Journal*, 936, 12
- Connaughton V., et al., 2015, *The Astrophysical Journal Supplement Series*, 216, 32
- D’Ai A., et al., 2017, GRB Coordinates Network, 21989, 1
- D’Elia V., et al., 2018, GRB Coordinates Network, 23229, 1
- D’Elia V., et al., 2023, GRB Coordinates Network, 33285, 1
- Evans P. A., et al., 2017, *Science*, 358, 1565
- Fermi GBM Team 2019, GRB Coordinates Network, 25240, 1
- Fermi GBM Team 2020, GRB Coordinates Network, 27363, 1
- Fermi GBM Team 2021, GRB Coordinates Network, 29232, 1
- Fermi GBM Team 2022a, GRB Coordinates Network, 31854, 1
- Fermi GBM Team 2022b, GRB Coordinates Network, 32820, 1
- Fermi GBM Team 2022c, GRB Coordinates Network, 33031, 1
- Fermi GBM Team 2023, GRB Coordinates Network, 34464, 1
- Frederiks D., et al., 2016, GRB Coordinates Network, 19554, 1
- Frederiks D., et al., 2017, GRB Coordinates Network, 21166, 1
- Frederiks D., et al., 2019a, GRB Coordinates Network, 23782, 1
- Frederiks D., et al., 2019b, GRB Coordinates Network, 25868, 1
- Frederiks D., et al., 2021, GRB Coordinates Network, 30694, 1
- Gibson S., et al., 2018, GRB Coordinates Network, 23097, 1
- Goldstein A., et al., 2017, *The Astrophysical Journal Letters*, 848, L14
- Gorski K. M., Hivon E., Banday A. J., Wandelt B. D., Hansen F. K., Reinecke M., Bartelmann M., 2005, *The Astrophysical Journal*, 622, 759
- Gupta S., et al., 2020a, GRB Coordinates Network, 27680, 1
- Gupta S., Vibhute V. S. A., Bhattacharya D., Bhalerao V., Rao A., Vadawale S., Collaboration A. C., et al., 2020b, GRB Coordinates Network, 28589, 1
- Hamburg R., Meegan C., 2017, GRB Coordinates Network, 21839, 1
- Hamburg R., Meegan C., Bissaldi E., Team F. G., et al., 2017a, GRB Coordinates Network, 21238, 1
- Hamburg R., Meegan C., Bissaldi E., Fermi GBM Team 2017b, GRB Coordinates Network, 21238, 1
- Harris C. R., et al., 2020, *Nature*, 585, 357
- Hložek R., 2019, *Publications of the Astronomical Society of the Pacific*, 131, 118001
- Hui C., 2017a, GRB Coordinates Network, 22289, 1
- Hui C. M., 2017b, GRB Coordinates Network, 22289, 1
- Hunter J. D., 2007, *Computing in Science & Engineering*, 9, 90
- Hurley K. C., 2020, *ApJ*, 905, 82
- Hurley K., et al., 2013, *The Astrophysical Journal Supplement Series*, 207, 39
- Hurley K., et al., 2019a, GRB Coordinates Network, 23764, 1
- Hurley K., et al., 2019b, GRB Coordinates Network, 25864, 1
- Kasliwal M. M., et al., 2017, *Science*, 358, 1559
- Kunszt P. Z., Szalay A. S., Thakar A. R., 2001, in *Mining the Sky: Proceedings of the MPA/ESO/MPE Workshop Held at Garching, Germany, July 31–August 4, 2000*. pp 631–637
- Kunzweiler F., Biltzinger B., Berlato F., Greiner J., Burgess J., 2020, GRB Coordinates Network, 27546, 1
- Landsman W. B., 1993, *Astronomical Data Analysis Software and Systems II*, 52
- Lien A., et al., 2016, *ApJ*, 829, 7
- Liu Z., et al., 2018, GRB Coordinates Network, 23125, 1
- Mailyan B., Hamburg R., Fermi GBM Team 2020, GRB Coordinates Network, 27550, 1
- Malacaria C., Hamburg R., Meegan C., 2018, GRB Coordinates Network, 23095, 1
- Malacaria C., Veres P., Meegan C., Bissaldi E., Fermi GBM Team 2020, GRB Coordinates Network, 29073, 1
- Mate S., et al., 2021, *Journal of Astrophysics and Astronomy*, 42, 1
- Meegan C., Fishman G., Wilson R., Paciesas W., Pendleton G., Horack J., Brock M., Kouveliotou C., 1992, *Nature*, 355, 143
- Mereghetti S., Götz D., Borkowski J., 2004, *Advances in Space Research*, 34, 2729
- Mészáros P., Fox D. B., Hanna C., Murase K., 2019, *Nature Reviews Physics*, 1, 585
- Mingo B., et al., 2016, GRB Coordinates Network, 19558, 1
- Mundell C., Guidorzi C., Steele I., 2010, *Advances in Astronomy*, 2010
- Nava L., Ghirlanda G., Ghisellini G., Celotti A., 2011, *A&A*, 530, A21
- Page K., Gropp J., Kuin N., Lien A., et al., 2021, GRB Coordinates Network, 30677, 1
- Piron F., 2016, *Comptes Rendus Physique*, 17, 617
- Poolakkil S., Meegan C., 2017, GRB Coordinates Network, 21992, 1
- Poolakkil S., Meegan C., Fermi GBM Team 2022, GRB Coordinates Network, 32830, 1
- Poolakkil S., Meegan C., Fermi GBM Team 2023, GRB Coordinates Network, 33288, 1
- Ridnaia A., et al., 2020, GRB Coordinates Network, 27398, 1
- Roberts O. J., Meegan C., Fermi GBM Team 2019, GRB Coordinates Network, 25248, 1
- Robitaille T. P., et al., 2013, *Astronomy & Astrophysics*, 558, A33
- Sakamaki A., et al., 2018, GRB Coordinates Network, 23547, 1
- Savchenko V., et al., 2017, *ApJ*, 848, L15
- Sharma Y., et al., 2021, *Journal of Astrophysics and Astronomy*, 42, 1
- Siegel M., Barthelmy S., Lien A., Page K., Palmer D., 2016, GRB Coordinates Network, 19830, 1
- Siegel M., et al., 2017, GRB Coordinates Network, 21821, 1
- Singh K. P., et al., 2014, in *Space Telescopes and Instrumentation 2014: Ultraviolet to Gamma Ray*. pp 517–531
- Stanbro M., Meegan C., 2016, GRB Coordinates Network, 19835, 1
- Stanbro M., Hui C., Meegan C., von Kienlin A., Team F. G., et al., 2017, GRB Coordinates Network, 21157, 1
- Svinkin D., et al., 2018, GRB Coordinates Network, 23128, 1
- Triou H., et al., 2009, in *Hard X-Ray, Gamma-Ray, and Neutron Detector Physics XI*. pp 169–177
- Tsvetkova A., et al., 2016, GRB Coordinates Network, 19511, 1
- Tsvetkova A., et al., 2018, GRB Coordinates Network, 23254, 1
- Ukwatta T., Beardmore A., Evans P., Gehrels N., Kennea J., Krimm H., Page K., Palmer D., 2016, GRB Coordinates Network, 19502, 1
- Ursi A., et al., 2020a, GRB Coordinates Network, 27685, 1



- Ursi A., et al., 2020b, GRB Coordinates Network, 28588, 1  
Veres P., Bissaldi E., 2018, GRB Coordinates Network, [23548](#), 1  
Veres P., Meegan C., 2016a, GRB Coordinates Network, 19901, 1  
Veres P., Meegan C., 2016b, GRB Coordinates Network, [19901](#), 1  
Vibhute A., Bhattacharya D., Mithun N. P. S., Bhalerao V., Rao A. R.,  
Vadawale S. V., 2021, [Journal of Astrophysics and Astronomy](#), **42**, 76  
Xin-Ying S., Wen-Xi P., Shuo X., Jin-Yuan L., Shao-Lin X., Qi L., Gang L.,  
Yue Z., 2020, SCIENTIA SINICA Physica, Mechanica & Astronomica,  
50, 129510  
Zhang B., 2014, [International Journal of Modern Physics D](#), **23**, 1430002  
von Kienlin A., et al., 2020a, [ApJ](#), **893**, 46  
von Kienlin A., et al., 2020b, [ApJ](#), **893**, 46

This paper has been typeset from a  $\text{\LaTeX}$  file prepared by the author.